Materials Science & Engineering A 802 (2021) 140671

Contents lists available at ScienceDirect

Materials Science & Engineering A

journal homepage: http://www.elsevier.com/locate/msea

Effect of different heat-treatment routes on the impact properties of an additively manufactured AlSi10Mg alloy

Maverick Giovagnoli [a,*], Marialaura Tocci [b], Annalisa Fortini [a], Mattia Merlin [a], Matteo Ferroni [c,d], Andrea Migliori [d], Annalisa Pola [b]

[a] University of Ferrara, Department of Engineering, Via Saragat 1, 44122, Ferrara, Italy
[b] University of Brescia, Department of Mechanical and Industrial Engineering, Via Branze 38, 25123, Brescia, Italy
[c] University of Brescia, Department of Civil Engineering, Architecture, Land, Environment and of Mathematics (DICATAM), Via Branze 43, 25123, Brescia, Italy
[d] CNR-IMM, Institute for Microelectronics and Microsystems, Via P. Gobetti 101, 40129, Bologna, Italy

ARTICLE INFO

Keywords:
Additive manufacturing
AlSi10Mg
Hot isotactic pressing
Heat treatment
Impact properties
Microstructural characterization

ABSTRACT

This work aims at investigating the impact behavior of an additively manufactured AlSi10Mg alloy subjected to different heat-treatment conditions. The commonly used heat-treatment routes were compared with a novel route (HPT6), which combines hot isostatic pressing (HIP), gas quenching, and ageing at high pressures. The as-built and treated alloy was characterized by Charpy impact testing and several microstructural and fractographic techniques, such as scanning electron microscopy, transmission electron microscopy (TEM), and X-ray diffraction. The as-built material displayed a very fine non-equilibrium microstructure, which led to a high impact strength but limited absorbed energy. Low-temperature annealing severely modified the starting microstructure of the alloy and restored its equilibrium condition. Even though this alloy did not suffer from strength loss, its absorbed energy increased significantly, resulting in an excellent impact performance. HIP application inhibited the growth of gas-hosting pores in the alloy when treated at high temperatures, yielding a material with a final relative density higher than 99%. TEM demonstrated that the novel HPT6 route induced precipitation strengthening in the alloy, thus increasing its impact strength when compared to the HIP route. Moreover, the HPT6 alloy and the alloy subjected to standard heat-treatment exhibited comparable impact performance. This suggests that the novel route proposed in this study can possibly replace the standard heat-treatment protocol, which would reduce the processing duration and cost of production of the additively manufactured AlSi10Mg alloy.

1. Introduction

Al–Si alloys are widely applied in many industrial fields, mainly for part production by foundry techniques. This is because the addition of Si reduces their melting temperature, results in a low shrinkage, and improves fluidity. It is known that small amounts of Mg in Al–Si alloys make them heat treatable and enhance their mechanical properties, thus enabling their application in structural components. In this alloy family, AlSi10Mg is ideal for high-performance applications that require lightweight materials with good corrosion resistance and weldability [1]. These properties, combined with its limited solidification range, make AlSi10Mg attractive for other manufacturing techniques as well.

In the last decade, an innovative production technology called additive manufacturing (AM) has been gaining importance in industrial and academic fields. Nowadays, many alloys can be manufactured using AM, including Al–Si alloys [2,3]. In particular, AlSi10Mg and AlSi12 alloys have been widely studied for this application, especially using the laser-based powder bed fusion (L-PBF) process [4], owing to their improved processability due to the high Si content. The solidification conditions in L-PBF are characterized by extremely high cooling rates and thermal gradients [5], which generally lead to an extra-fine microstructure, which is in strong contrast with the microstructure obtained using conventional technologies [6]. In detail, the presence of fine primary Al-cells surrounded by a network of Si is typical in the above-mentioned Al–Si alloys [4]. In addition, high cooling rates are responsible for a high degree of supersaturation of Si in Al-cells [7,8]. Furthermore, it was found that fine Si particles and Mg_2Si precipitates are present in the Al matrix [6,7], together with a system of entangled

* Corresponding author.
E-mail address: maverick.giovagnoli@unife.it (M. Giovagnoli).

https://doi.org/10.1016/j.msea.2020.140671
Received 15 September 2020; Received in revised form 24 November 2020; Accepted 12 December 2020
Available online 15 December 2020

dislocations [6]. These aspects contribute to material strengthening via different routes, such as solid-solution strengthening, the Hall-Petch effect, and Orowan strengthening, leading to high mechanical properties in L-PBF Al–Si alloys, especially in terms of their strength and hardness [7].

Heat treatment is a fundamental post-processing step for these alloys, as well as for other metallic materials, to ensure that the material performance is adequate for the considered application. Specifically, high-performance as-built alloys Al–Si alloys produced by L-PBF suffer from high residual stresses and anisotropy, thus necessitating heat treatment. In this regard, many researchers have investigated the effect of heat-treatment parameters on the microstructural and mechanical properties of Al–Si alloys. In the case of AlSi10Mg, two main heat-treatment paths can be identified. The first one relates to low-temperature treatment (annealing or stress relieving; typically performed at 300 °C for 2 h) to remove internal residual stresses [9]. Recently, it has been shown that it is necessary to decrease the stress-relieving/annealing temperature to minimize microstructural coarsening [10,11].

The second approach is related to T6 treatment, which is a more traditional heat-treatment route for Al–Si–Mg alloys [7,12,13]. This approach allows the removal of internal residual stresses and reduces material anisotropy, which can be detrimental to material performance. Meanwhile, the high temperatures involved in solution treatment lead to coarsening of the extra-fine microstructure obtained after solidification, which can lead to a loss in material strength besides altering the unique features obtained by AM. An additional drawback of this method is the growth of pores at high temperatures [14,15].

To counteract porosity development during solution treatment, hot isostatic pressing (HIP) is frequently performed before T6 treatment [16–18]. The beneficial effects of HIP on the microstructural quality of alloys due to pore closure and densification as well as their tensile and fatigue properties have been discussed in several studies [16,17]. However, it should be noted that HIP is not very effective when the as-built material is poor in quality (low density), which is a result of using non-optimized process parameters [19,20].

Interestingly, the temperature range of HIP is similar to that used for solution treatment. Therefore, combining these two steps (HIP and solution treatment) in a single high-pressure treatment process may be viable. Based on this premise, in this investigation, a novel high-pressure T6 (HPT6) heat treatment is proposed, which involves rapid quenching and ageing at a high pressure. A similar treatment was performed on casting A356 alloys [21] and positive results were observed in terms of strength and fatigue resistance; the effectiveness of this method in combination with AM has recently been explored by the authors in preliminary investigations [22]. Furthermore, pore regrowth has been reported during heat treatment after HIP [23], which is an additional reason to maintain high pressures during the entire treatment cycle.

Therefore, in the present study, the effect of various heat-treatment protocols was studied, including annealing, T6, HIP only, HIP followed by T6, and HIP followed by ageing at a high pressure (HPT6). Our aim was to compare the results of the most used heat-treatment routes with those obtained using the innovative high-pressure T6 heat-treatment protocol. The evolution of microstructural properties was investigated to understand the influence of the applied pressure. Furthermore, material densification was measured and the mechanical response of the treated alloys was studied by Charpy impact testing. This allowed us to analyze alloy behavior during rapid loading as it represents a fundamental property for the design of components. In general, few studies have been performed on the impact behavior of L-PBF AlSi10Mg alloys [20,24–26], with none focused on the effect of HPT6 on the impact properties of these materials. Additionally, impact loading is particularly sensitive to material porosity, which can decrease its ability to absorb energy. Therefore, impact behavior is considered to be a particularly suitable parameter to evaluate the effectiveness of the proposed post-processing route.

Table 1
Chemical composition (wt.%) of the AlSi10Mg alloy produced by L-PBF.

Si	Mg	Fe	Mn	Cu	Al
10.245 ± 0.091	0.396 ± 0.001	0.213 ± 0.002	<0.002	<0.002	balance

2. Experimental

2.1. L-PBF and heat treatment

Impact strength specimens (12 × 12 × 57 mm^3) were produced from a commercial EOS AlSi10Mg powder (EOS GmbH Electro Optical Systems, Krailling, Germany) with their long sides parallel to the building platform. The powder was subjected to L-PBF in a protective Ar atmosphere on an EOS M290 system (laser power 400 W and 100 μm focus diameter; other parameters cannot be disclosed as this study was performed in collaboration with industry [20]). Table 1 shows the chemical composition of the AlSi10Mg alloy thus produced. The values shown were evaluated by optical emission spectrometry.

The specimens were subjected to HIP treatment at different pressures on a Quintus Technologies instrument (Västerås, Sweden). HIP_{50} and HIP_{150} refer to HIP treatment at pressures of 50 and 150 MPa, respectively. In addition, some of the samples were subsequently heat-treated (T6), as shown in Table 2 to yield HIP_{50} + T6 and HIP_{150} +T6 specimens. In the new HPT6 protocol, the samples were directly quenched inside the HIP vessel using a cooling gas and then reheated to the ageing temperature while maintaining high-pressure conditions. The cooling rate provided by the QIH 21 M Uniform Rapid Quenching (URQ®) unit was ~7 K/s between 540 °C and 200 °C, whereas a typical cooling rate of HIP systems is ~0.2 K/s [21]. Additional details on the working principle of the URQ® unit can be found elsewhere [21]. $HPT6_{50}$ and $HPT6_{150}$ refer to high-pressure T6 treatment at 50 and 150 MPa, respectively. For comparison, specimens in the as-built, annealed, and conventional T6 heat-treated (without the HIP) conditions were also tested. Annealing and T6 treatments were performed in laboratory furnaces at atmospheric pressure using the time and temperature values listed in Table 2.

After heat treatment, the alloys were machined to yield standard sized Charpy specimens (10 × 10 × 55 mm^3) according to the ASTM E23 standard. A U-notch was realized on the top surface of the specimens.

2.2. Density measurement and mechanical properties

To analyze densification in the specimens due to HIP treatment, density measurements were conducted on 10 × 10 × 55 mm^3 Charpy impact specimens using Archimedes' method. The samples were first weighed in air followed by measurement in distilled water; to measure sample weight, a Gibertini Europe 500 (Novate Milanese, Italy) analytical digital balance was used. At least three specimens were employed for each heat-treatment condition and their averages and standard deviations were calculated. Relative density was calculated as a percentage of the nominal alloy density (~2.68 g/cm^3). Hardness measurements were performed on one Charpy specimen for each heat-treatment route. An LTF Galileo Ergotest Comp 25 (Antegnate, Italy) hardness machine with a 2.5 mm diameter spherical indenter was used for hardness testing using a 613 N load, which was applied on the specimen for 15 s. Four indentations were performed on each sample and their average and standard deviation values were calculated.

Charpy impact tests were performed at room temperature (25 °C) with a CEAST Resil Impactor (Instron-CEAST, Pianezza, Italy) instrumented pendulum (50 J of available energy). Impact test data was recorded on a CEAST DAS 64 K system and the corresponding force-displacement curves were generated according to ISO 14556:2015 standards. This data was further analyzed using a tailored Matlab® code to determine the relevant parameters of the acquired curves [26]: peak force (F_P, [kN]), the maximum recorded force value; initiation energy (E_I, [J]), the area below

the force-displacement curve up to the peak force; propagation energy (E_P, [J]), the area below the force-displacement curve beyond the peak force.

2.3. Microstructural characterization

The tested Charpy specimens were cut perpendicular to the U-notch to obtain transversal sections for microstructural investigation. The samples were prepared according to standard metallographic protocols and finished using an oxide polish suspension. Image of Fe-based intermetallic compounds and Si phases was conducted on ten micrographs of the as-polished samples to avoid artifacts resulting from etching. Equivalent diameter (ED) [27] and width were measured as representative size parameters for Si particles and Fe-based compounds, respectively. Additionally, the area fraction of Fe-rich compounds was measured. The samples were then etched for 10 s with a 0.5 wt% HF aqueous solution. Fractographic and microstructural characterization was conducted using a Zeiss EVO MA 15 (Oberkochen, Germany) scanning electron microscope (SEM) equipped with an Oxford X-Max 50 (Oxford Instruments, Abingdon-on-Thames, UK) energy-dispersive X-ray (EDX) probe.

Precipitation strengthening after the novel HPT6 treatment was verified by transmission electron microscopy (TEM). The alloy treated at 150 MPa was chosen as the reference. In this case, 3 mm-diameter disk samples were first mechanically thinned and polished to a thickness of ~25 μm. Final thinning was performed by low-energy Ar^+ ion-beam milling on a GATAN precision ion polishing system. TEM images were recorded on a FEI Tecnai F20 (FEI Company, Hillsboro, USA) TEM operating at 200 keV. Bright-field (BF) imaging, selected area electron diffraction (SAED), and high-resolution electron microscopy were conducted to analyze the presence of hardening compounds.

X-ray diffraction (XRD) tests were conducted using the Bragg-Brentano geometry on a Bruker D8 Advance (Billerica, USA) diffractometer equipped with a Cu filament (Kα, 1.5406 Å). All patterns were acquired in the 2θ range of 20°–110° with a step-size of 0.02° and step time of 1 s. Full-pattern analysis was conducted using Maud software [28]. The volumetric fraction of the Si phase was computed by Rietveld refinement based on the relative intensities of Si and Al reflections. The Al phase lattice parameter was additionally calculated by Rietveld refinement and compared with the one calculated using the $\cos^2(\theta)/\sin(\theta)$ method on the full pattern.

Table 2
Experimental conditions for AlSi10Mg alloy treatment.

Designation	HIP (+argon quench)	Solution treatment (+water quench)	Ageing	Annealing
as-built	–	–	–	–
annealed	–	–	–	300 °C, 2 h
T6	–	520 °C, 2 h	180 °C, 4 h	–
HIP_{50}	520 °C, 2 h, 50 MPa	–	–	–
$HPT6_{50}$	520 °C, 2 h, 50 MPa	–	180 °C, 4 h, 50 MPa	–
HIP_{50} + T6	520 °C, 2 h, 50 MPa	520 °C, 2 h	180 °C, 4 h	–
HIP_{150}	520 °C, 2 h, 150 MPa	–	–	–
$HPT6_{150}$	520 °C, 2 h, 150 MPa	–	180 °C, 4 h, 150 MPa	–
HIP_{150} + T6	520 °C, 2 h, 150 MPa	520 °C, 2 h	180 °C, 4 h	–

3. Results and analysis

3.1. Microstructural investigation

The SEM images in Fig. 1 show the morphological and compositional features of the microstructure of the as-built alloy. In the secondary electron (SE) image of the transverse section (Fig. 1a), a dotted line is used to highlight the typical semi-circular shape of laser scan tracks, which range between 100-150 and 60–80 μm in width and depth, respectively. Fig. 1b, taken from the area marked with the solid line in Fig. 1a, shows that the melt pools consist of a continuous network of eutectic Si surrounding Al cells with the latter exhibiting a different morphology. Inside the melt pool, Al cells are mainly elongated along the building direction, with a width of 300–500 nm and length of a few μm. In contrast, in the proximity of the melt-pool boundary, Al cells are mostly equiaxed in the submicron range. In Fig. 1c, the back-scattered electron (BSE) image complements the observations in Fig. 1a and provides a crystallographic contrast. Elongated grains, 5–10 μm wide and several tens of μm long, are present inside the melt pool. Meanwhile, finer equiaxed grains, ~10 μm in size, were located along the melt-pool boundary. The morphology of the small Al cells seems to be strongly related to that of grains, even though their size is at least one order of magnitude smaller.

In the annealed alloy shown in Fig. 2a, scan tracks were not very visible because of the broken Si network [10], resulting in separate small Si particles with a calculated ED of 92 nm. In addition, sparse pores in a section of the sample appear as dark features in the SE image. Fig. 2b, which is an image corresponding to the area marked with the solid line in Fig. 2a, highlights that Si particles are slightly coarser at the melt-pool boundary than in the inner region. This implies that the melt pool is still discernible after annealing, as highlighted by the dotted line in Fig. 2a. Fig. 2c confirms that the Al grains maintain a columnar shape inside melt pools and an equiaxed shape at pool boundaries. Finally, it can be stated that low-temperature annealing did not significantly increase the grain size [29].

Fig. 3a-b-c show the microstructure of the AlSi10Mg alloy after HIP_{150} treatment (chosen as a representative of the HIP_{50}, HPT6, and HIP + T6 conditions). It can be seen in Fig. 3a that the Si particles are significantly coarsened when compared to those in the annealed alloy. As can be seen in Fig. 3b, elongated Al grains do not show remarkable differences in size when compared to those in as-built and annealed alloys [29]. Fig. 3c shows that the large Si particles mainly originate from the breaking up of the eutectic Si network and are mostly located at the boundaries of Al grains. In addition, the nucleation of nanometric Si particles was observed inside Al grains originating from the supersaturated Si solid solution of the as-built state [30]. While HIP treated samples do not show appreciable porosity, coarse pores 10–20 μm wide are clearly visible as dark features in the T6 sample (Fig. 3d), with the regular shape suggesting them to be gas pores.

Mainly acicular features, a few hundreds of nm in width and up to several μm in length (Fig. 3c), could be observed in all of the considered heat-treatment conditions. EDX measurements revealed them to be Fe-rich compounds, with $Al_{4.5}Si_{1.5}Fe_{1.5}$ as the likely stoichiometric composition. Such a composition is quite similar to the β-Al_5SiFe phase, a plate-shaped Fe-bearing intermetallic compound reported to be found in AlSiMg(Fe) cast [31] and AM [7] alloys. Permanence at high temperatures leads to the coarsening of β-Al_5SiFe compounds, which were likely formed at the boundaries of Al cells during solidification as extra-fine particles due to high cooling rates [6,32].

As previously stated, SEM images of all samples heat-treated at a high temperature showed microstructural features similar to those visible in Fig. 3, apart from gas pores of the T6 sample. The calculated ED of Si particles by image analysis ranged between 1.1 and 1.2 μm for T6, HIP, and HPT6 alloys. This elucidates the negligible effect of the ageing treatment on coarsening of micrometric features owing to its low temperature [33], although it promotes the precipitation of nanometric

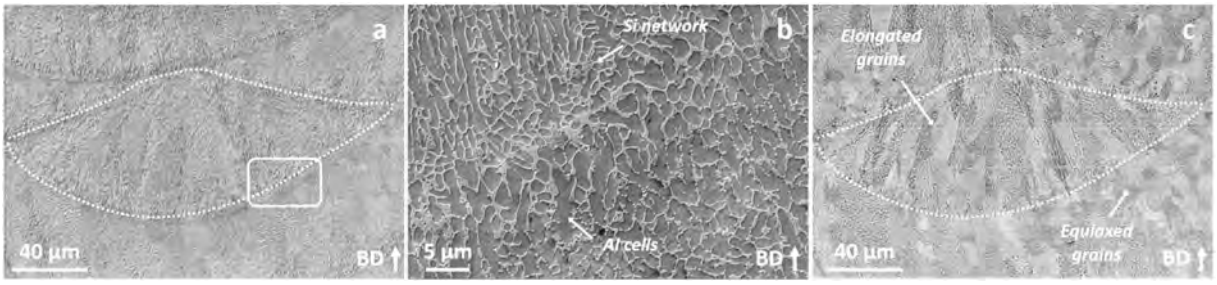

Fig. 1. SEM images of a melt pool in the transverse section of the as-built AlSi10Mg alloy. (a) Panoramic SE image revealing the semi-circular shape of the melt pool, with boundaries marked by the dotted line and the white arrow showing the building direction (BD). (b) Detailed image taken from the area marked by the solid line in (a), with eutectic Si network and Al cells with a different morphology at the boundary. (c) BSE image with crystallographic contrast highlights the grain structure in the melt pool, and the dotted line underlines the melt pool boundaries of the same area as (a).

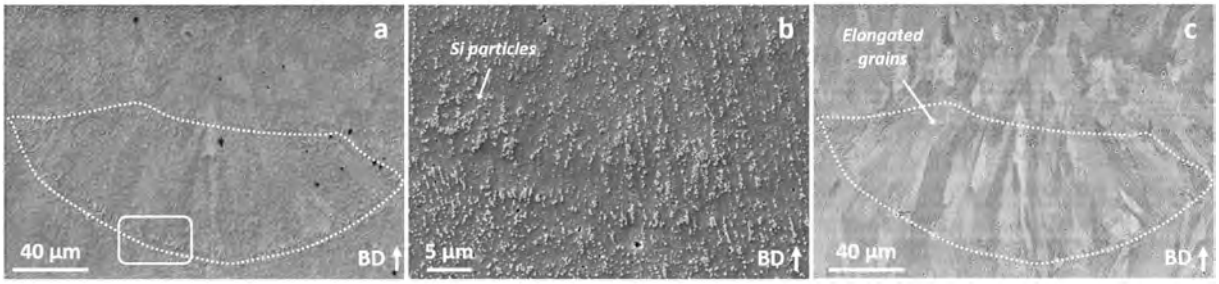

Fig. 2. SEM images of a melt pool in the transverse section of the annealed AlSi10Mg alloy. (a) Panoramic SE image revealing the semi-circular shape of the melt pool, with boundaries marked by the dotted line and the white arrow showing the building direction (BD). (b) Detailed image taken from the area marked by the solid line in (a), with nanometric Si particles with different size at the boundary. (c) BSE image shows the crystalline structure in the melt pool, and the dotted line underlines the melt pool boundaries of the same area as (a).

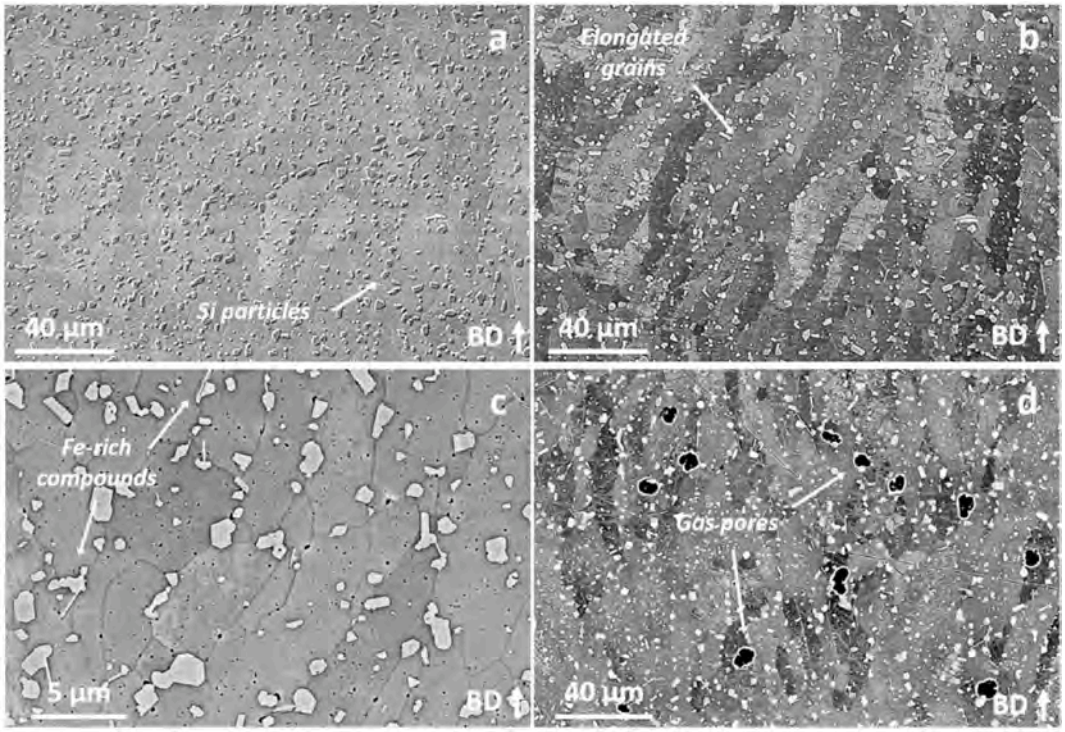

Fig. 3. SEM images in the transverse section of the AlSi10Mg alloy after HIP_{150} (a-b-c) and T6 (d) treatments. (a) SE image shows micrometric Si particles, and the white arrow shows the building direction (BD). (b) BSE image of the same area as (a) shows elongated grains by crystallographic contrast. (c) distribution of Si particles in the grains and along the grain boundaries, presence of acicular Fe-rich compounds. (d) BSE image shows coarse gas pores as dark features.

compounds not visible in SEM images. The longer permanence at high temperatures slightly coarsened the Si particles of HIP50 + T6 and HIP150 + T6 samples up to the range of 1.38–1.56 μm. Even if a reduced atomic diffusivity could be expected as the applied pressure increases (0.1, 50 and 150 MPa), results of image analysis indicated that pressure does not appreciably affect the microstructure at the micrometric scale [22]. Likely, the increased diffusivity at high temperatures overcomes such a drawback, which makes the total exposure at high temperatures the main parameter affecting the microstructural evolution of the alloy.

Regarding the Fe-bearing compounds, they had a comparable width for T6, HIP, and HPT6 samples, whereas they slightly coarsened in HIP + T6 samples, matching the observation of Si particles. Their area fraction ranged between 0.66 and 0.83% for all investigated samples, suggesting that the equilibrium condition was achieved.

Fig. 4 shows the results of TEM analysis conducted to evaluate precipitation strengthening after $HPT6_{150}$ treatment. The BF TEM image in Fig. 4a shows the microstructure of the alloy at a low magnification. Large features like Si particles and acicular Fe-rich compounds were found to be embedded in the Al matrix and present a dark contrast due to crystalline diffraction.

Fig. 4b shows local modulation in the BF contrast of the Al phase and suggests that the Al matrix is divided into several sub-domains ranging from a few tens of nanometers to a few hundreds of nanometers in size. According to literature [33–35], the brighter areas in Fig. 4b represent dislocation-free Al sub-grains or cells and these are separated by darker areas that represent heavily defective zones. As depicted in Fig. 4c, these latter may represent Al sub-grains with a high density of dislocations or dislocation tangles, which form dense dislocation walls along the boundaries of neighboring sub-grains.

Fig. 4d shows the SAED pattern corresponding to the area in Fig. 4b. The squared pattern of intense spots corresponds to the Al crystal structure aligned along the $[001]_{Al}$ zone axis. The circular shape of $[020]_{Al}$-Bragg reflections appear slightly distorted, indicating that dislocation tangles gathered and had a small angular misorientation between boundaries [34,35].

The red arrows highlight additional weak spots in the squared Al pattern, suggesting that ageing induces the formation of strengthening compounds. Some investigators reported that nanometric Si particles precipitate in AM produced Al alloys, given the high degree of supersaturation in the as-built state [7,29]. Additionally, several Mg-bearing compounds are reported in the precipitation sequence of aged Al–Mg–Si alloys [36–38]. Analysis of these additional spots, based on crystallographic data available in the literature, was conducted considering the associated d-spacing and their mutual orientation. The results of this analysis do not agree with the Si phase but concur with the results of hexagonal B′-$Mg_9Al_3Si_7$ [38] and monoclinic β′′-Mg_5Si_6 [37,39] phases. The latter is commonly associated with peak-aged Al–Mg–Si alloys while the former is usually reported in over-aged alloys and in AM produced A357 alloys subjected to ageing after a short (1 h) solution heat treatment [40].

Crystallographic interpretation of the SAED pattern suggests the formation of precipitates within Al crystals, with a coherent orientation with respect to the matrix, and this requires further observations of the Al lattice at a high magnification. The high-resolution TEM (HRTEM) image in Fig. 4e shows a set of contrast fringes superimposed on the [100]-oriented Al lattice. Based on the fast-Fourier transform (FFT) of the HRTEM image in Fig. 4f, an analysis of spatial frequencies shows that this set of fringes corresponds to a lattice with a 2.21 Å spacing oriented at 23° along the $[020]_{Al}$ direction. The spatial frequencies circled in Fig. 4f represent sets of planes with spacing in the range of 2.21–4.81 Å

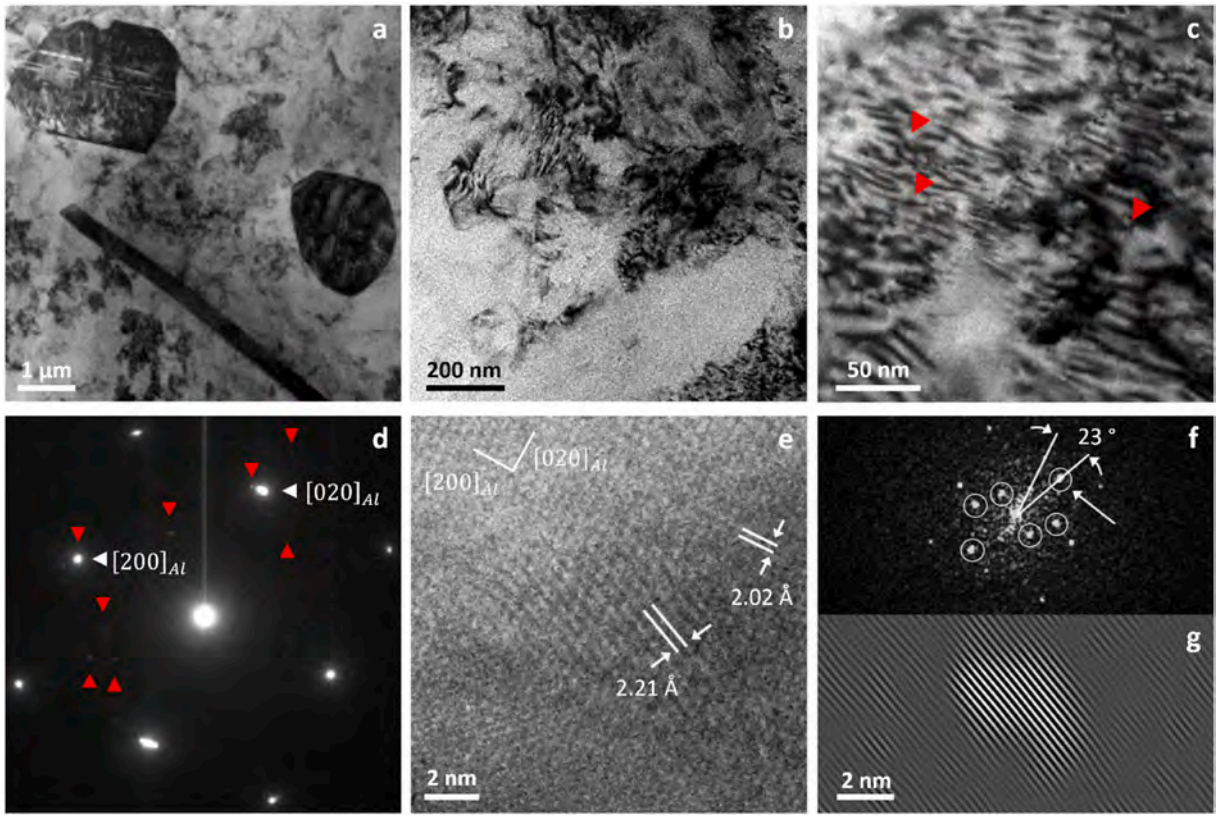

Fig. 4. TEM observations of the $HPT6_{150}$ alloy. (a) BF TEM micrograph of Si particles and acicular Fe-rich compound. (b) Al domains with dislocation tangles in their interior. (c) Dense dislocation tangle separating adjacent Al domains. (d) SAED pattern of (b), red arrows show reflections matching with the ageing-induced precipitates. (e) HRTEM micrograph of the fringe pattern tilted to the matrix. (f) FFT of (e) showing spatial frequencies in the Al squared pattern. (g) Inverse FFT using the frequency pointed at by an arrow in (f) showing the presence of a precipitate. (For interpretation of the references to colour in this figure legend, the reader is referred to the Web version of this article.)

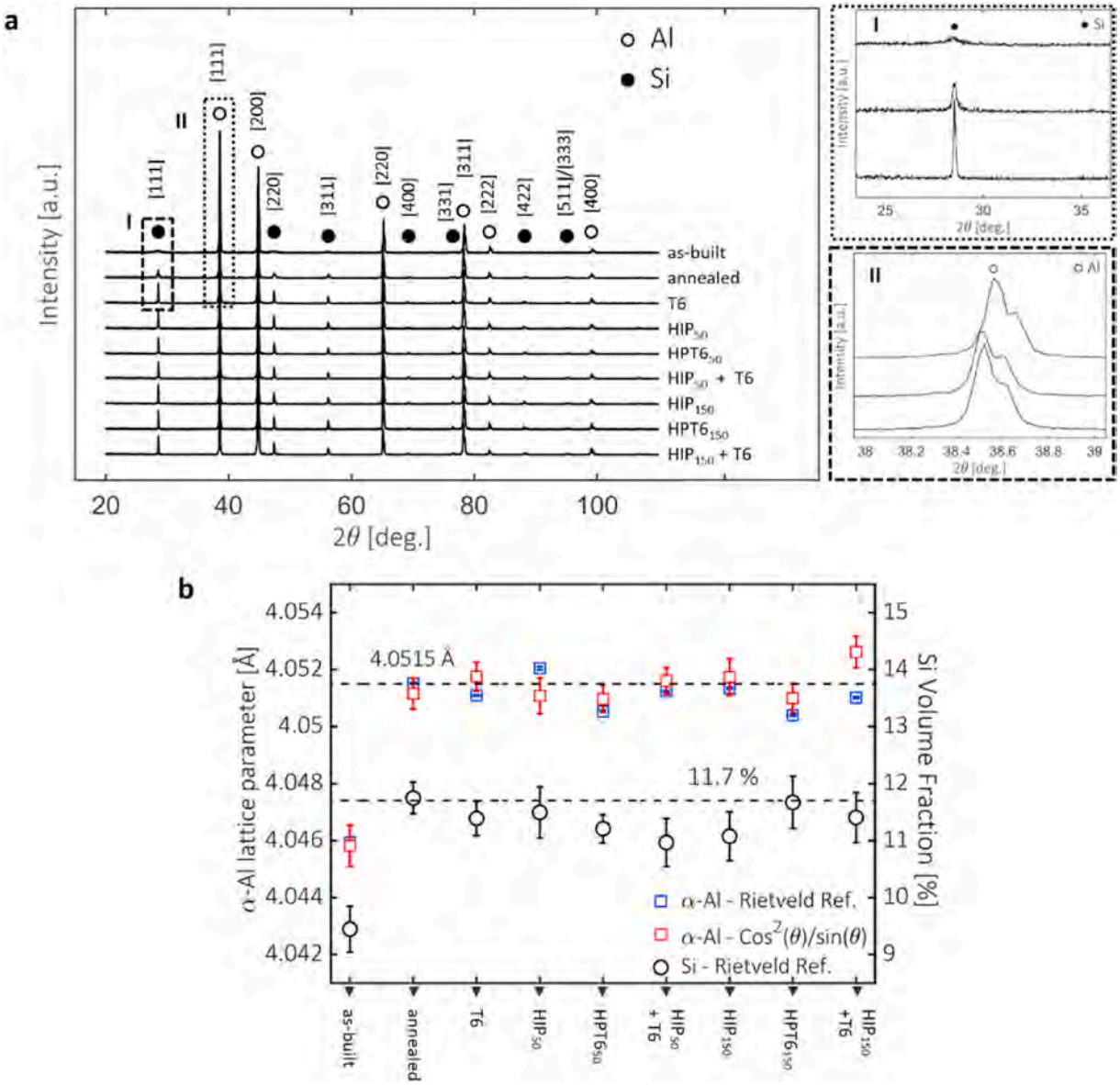

Fig. 5. XRD of the AlSi10Mg alloy in different heat-treatment conditions. (a) Full pattern highlighting the Al and Si reflections, inset I shows the broadening of Si peaks, inset II shows the shift of Al peaks. (b) α-Al lattice parameter and Si volume fraction, the error is presented as the estimated standard deviation.

and they do not correspond to the Al fringe pattern or to possible Si reflections. In agreement with the SAED pattern, such spatial frequencies correspond to the B′-$Mg_9Al_3Si_7$ and β′′-Mg_5Si_6 phases. Fig. 4g shows an inverse masked FFT generated using the frequency pointed at by an arrow in Fig. 4f, showing the presence of a small component 4–5 nm in size. TEM investigation reveals other similar features, all with sizes in the range 4–10 nm and closely matching either B′-$Mg_9Al_3Si_7$ or β′′-Mg_5Si_6 phases.

It is worth noting that the reported TEM results do not help us in unambiguously determining the nature of the ageing-induced precipitates; however, this aspect is beyond the scope of this study. Nevertheless, it can be demonstrated that the novel combination of HIP and ageing treatment under pressure is capable of inducing precipitation strengthening in AlSi10Mg alloys.

3.2. XRD analysis

Fig. 5a shows the full XRD patterns corresponding to each investigated condition; in these patterns, only Al and Si phases could be detected. Even though Mg-based compounds were expected to precipitate after ageing treatment in AlSi10Mg alloys, none of the aged specimens showed the corresponding reflections.

Inset I in Fig. 5a illustrates that Si reflections display a broadened peak with reduced intensity in the XRD patterns of the as-built and annealed samples when compared to the patterns of high-temperature heat-treated specimens. The former indicates that Si crystalline domains gradually increase in size, starting from the as-built state. Moreover, the ratio between the integral area of Si reflections and integral area of all detected reflections (*i.e.*, Al and Si) represents the volume fraction of Si. Hence, the increased intensity of Si reflections after heat treatment suggests a gradual increase in the total Si content.

In the as-built condition, Al reflections shifted to higher 2θ angles, which means lower Al lattice parameters as described by the Bragg equation. Inset II in Fig. 5a, which displays such features for the Al [111] reflection, was considered as the reference and the heat-treated specimens were analyzed with respect to this reference. Distortion in the

Table 3
Characteristic impact toughness parameters and Brinell hardness.

	Relative Density [%]	F_P [kN]	E_I [J]	E_P [J]	Hardness [HBW]
as-built	99.8 ± 0.2	6.8 ± 0.07	2.6 ± 0.1	2.1 ± 0.09	125 ± 1
annealed	99.1 ± 0.1	6.9 ± 0.03	7.8 ± 0.10	11.3 ± 0.16	87 ± 1
T6	97.9 ± 0.3	6.4 ± 0.20	2.3 ± 0.35	0.4 ± 0.06	104 ± 1
HIP_{50}	99.5 ± 0.1	5.4 ± 0.14	5.8 ± 0.39	5.0 ± 0.09	79 ± 1
$HPT6_{50}$	99.5 ± 0.1	6.6 ± 0.06	3.3 ± 0.01	1.6 ± 0.14	100 ± 1
HIP_{50} + T6	99.2 ± 0.1	6.6 ± 0.03	3.0 ± 0.08	0.6 ± 0.04	99 ± 2
HIP_{150}	99.4 ± 0.2	5.4 ± 0.22	5.5 ± 0.48	4.6 ± 0.09	83 ± 1
$HPT6_{150}$	99.5 ± 0.2	6.8 ± 0.19	3.4 ± 0.08	1.1 ± 0.09	104 ± 1
HIP_{150} + T6	99.4 ± 0.1	7.2 ± 0.17	3.0 ± 0.54	0.7 ± 0.16	111 ± 1

phase lattice produces a shift in the corresponding reflections due to either microstructural (*e.g.*, altered solid solution) or mechanical (*e.g.*, residual stresses) effects. Fig. 5b shows the lattice parameters calculated for the Al phase in each condition. The results obtained from Rietveld refinement and the $\cos^2(\theta)/\sin(\theta)$ method are in agreement with each other. Both confirm that the as-built alloy exhibits the lowest lattice parameter of 4.0459 and 4.0458 Å for the two methods, respectively. After each heat treatment, this value increases more or less to the equilibrium value, which for Al in AlSi10Mg alloys is reported to be 4.0515 Å [41]. The disappearance of Al lattice distortions suggests that such distortion is a process-related alteration quickly recovered after heat treatment, even with low-temperature annealing.

Fig. 5b also reports the Si volumetric fraction calculated using the Rietveld method. In agreement with Al lattice-parameter analysis, the as-built alloy showed the lowest Si volumetric fraction of ~9.4%, which reflects the low intensity of Si reflections. After heat treatment, all the calculated values were close to the equilibrium value of 11.7%. Hence, unlike in the as-built state, the reduced intensity of Si peaks in the annealed alloy is not related to a low Si volumetric fraction, as the integral breadth of the peaks is similar to that in other heat-treated conditions. Therefore, the widening of Si peaks can be ascribed to the small particle size of Si in the range of a tens of nanometers, which mirrors the results of microstructural investigation (Fig. 2b).

3.3. Density and mechanical properties

Density measurements were conducted to analyze the actual densification effect of HIP treatment. Table 3 reports the results obtained in terms of relative density. In the as-built condition, the alloy was almost completely dense with a relative density of 99.8%. Conversely, conventional T6 heat treatment reduced the relative density to 97.9%. These values were considered as the upper and lower thresholds for evaluating the effectiveness of the HIP process. Despite the low temperature employed, annealing reduced the relative density to 99.1%, corresponding to the appearance of pores in Fig. 2a. However, even though their relative densities were lower than that of the as-built alloy, all the HIP treated alloys showed values greater than 99%, thus confirming the densification effect of HIP treatment [20]. Furthermore, there were no significant differences in the relative density when the pressure was changed from 50 to 150 MPa.

Table 3 also shows the impact parameters calculated from the Charpy force-displacement curves in Fig. 6 and the results of Brinell hardness tests. The as-built alloy was characterized by its high strength; the calculated peak force value F_P of ~7 kN is much higher than that previously reported for cast AlSiMg alloys [26] and agrees with an outstanding hardness value of ~125 HBW. Nevertheless, this alloy suffers from a poor total absorbed energy (*i.e.*, area under the force-displacement curve, 4.7 J), which is equally divided between crack initiation (E_I) and propagation (E_P) stages. Regardless of the pressure level, HIP application only softened the material. It enhanced E_I and E_P by a factor 2 when compared to the initial state but reduced the impact strength by ~20% to 5.4 kN. Similarly, the hardness of the alloy reduced to ~80 HBW.

The HPT6 and HIP + T6 alloys displayed F_P and hardness values closer to the as-built state (6.6–7.2 kN and 100–110 HBW, respectively). The absorbed initiation energy E_I was slightly higher (3.0–3.4 J) and this was accompanied by a remarkable drop in E_P (0.6–1.5 J). In addition, this decrease was slightly higher in HIP + T6 alloys than in HPT6 alloys. The characteristic impact parameters of T6 alloys follow similar trends, but each of them is the lowest in the corresponding category when compared to the rest of the alloys subjected to different ageing-treatment conditions. The enhanced ductility of the annealed alloy increased its E_I and E_P by a factor of 3 and 5, respectively, when compared to the initial state. Interestingly, the impact strength of the annealed alloy is almost the same as that of the as-built alloy, while its hardness reduced by ~30%, from 125 to 87 HBW.

3.4. Fractographic investigation

Fig. 7 shows the fracture surfaces of the as-built alloy, in which the outlines of melt-pool sections are readily detectable (Fig. 7a). Previous studies [26] reported that such features are typical of L-PBF horizontally oriented samples and classified them as *trans-track* fractures. The moderate flatness of the fracture surface at a low magnification suggests brittle fracture behavior. Fig. 7b shows several emerging ridges, mostly elongated along the preferred orientation of grains and cells (Fig. 1a). At higher magnifications (Fig. 7c), it can be observed that these ridges emerge from Al cells to form fine irregular dimples and host continuous stripes of the Si network.

The SE images in Fig. 8 show details of the fracture surface of the annealed alloy. Footprints of the scan tracks are still detectable, as underlined in Fig. 8a. The higher magnification image in Fig. 8b indicates the presence of features such as fine equiaxed dimples that could not be observed in the as-built sample. Fig. 8c shows that each dimple hosts nanometric Si particles, as previously noted in Fig. 2b. Such isolated Si particles promote the development of micro-voids, resulting in the formation of several dimples during deformation and suggest a ductile fracture behavior.

Fig. 9 shows characteristic fracture surfaces of the alloy heat-treated at a high temperature. Coarse, equiaxed, and deep dimples, several microns in size, appear on the fracture surfaces of HIP treated alloys, as shown in Fig. 9a, suggesting ductile fracture behavior. Compared to the fine dimples seen in the annealed alloy (Fig. 8b), the dimples in HIP-ed alloys are approximately one order of magnitude larger in size. This feature is consistent with the coarsening of Si particles (Fig. 3a) during the heat treatment of AlSi10Mg alloys at high temperatures. At higher magnifications (Fig. 9b), both Si particles and Fe-rich compounds are detected inside the dimples, as confirmed by EDX analysis.

Fig. 9c depicts a representative fracture surface of the alloys subjected to ageing as the final step of the heat-treatment process. Compared to the HIP-ed alloy, shallow and smaller dimples appear, together with many secondary cracks in brittle secondary phases. This accounts for the highly brittle fracture behavior of the aged alloys, as expected from the formation of strengthening compounds. The EDX map in Fig. 9d highlights the presence of a large number of Si particles and cracked Fe-compounds, which can be observed in Fig. 9b. Porosity was not significant on the fracture surfaces of HIP-ed samples, which indicates successful densification. However, pores were present on T6 surfaces, as documented by our research team in a previous study [26].

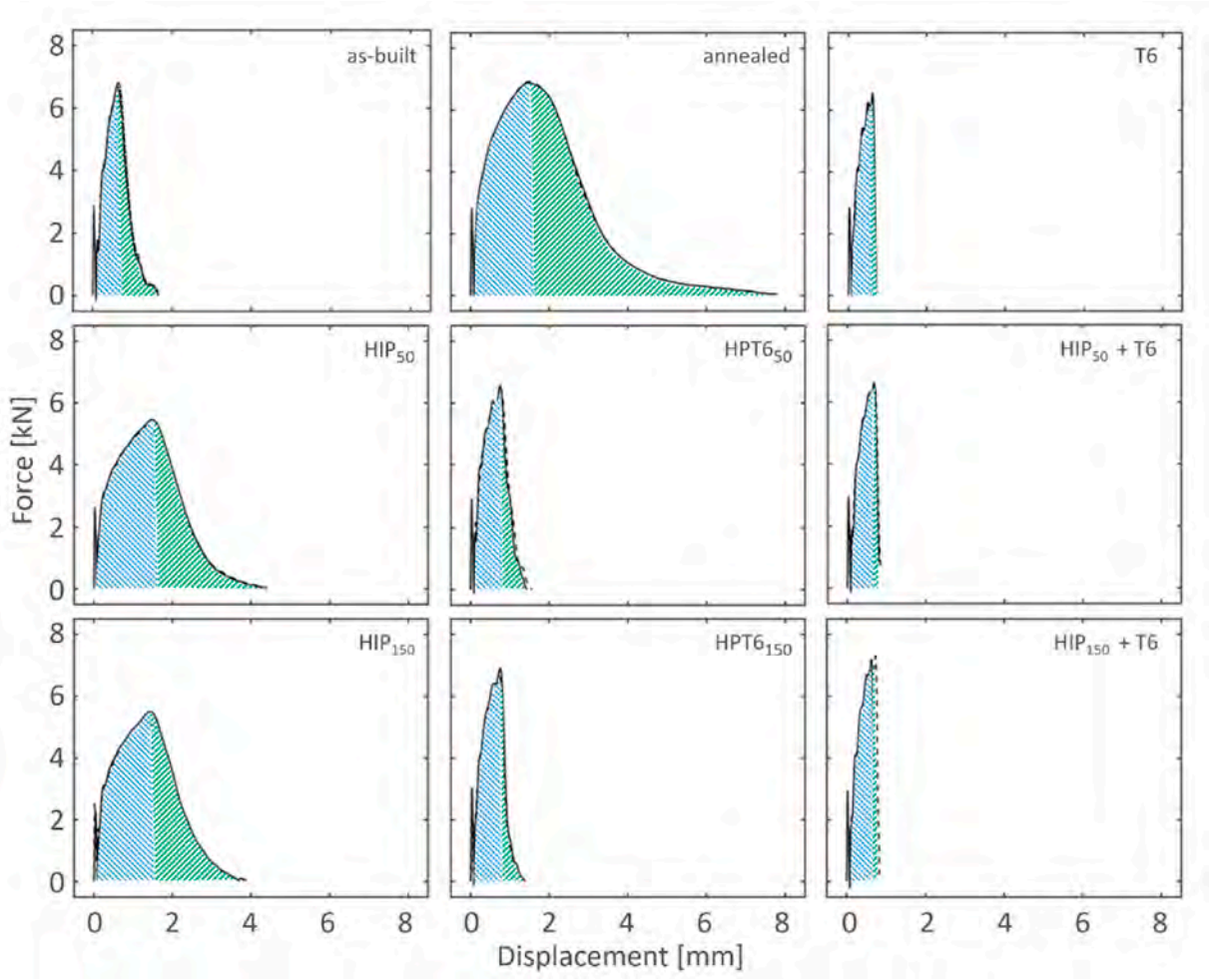

Fig. 6. Force-displacement curves from Charpy impact tests of the alloy in different heat-treatment conditions. Areas marked in blue and green correspond to initiation (EI) and propagation (EP) energies, respectively. Solid and dashed lines show the reproducibility of the results of different tested samples. (For interpretation of the references to colour in this figure legend, the reader is referred to the Web version of this article.)

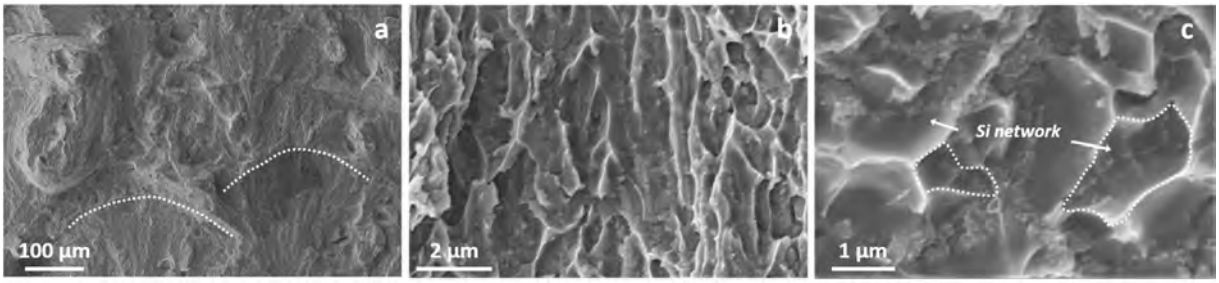

Fig. 7. Fracture surface of the AlSi10Mg alloy in the as-built condition (SE images). (a) panoramic view of the surface, the dotted lines show traces of the melt pool boundaries. (b) Elongated ridges. (c) Irregular dimples and traces of the Si network.

4. Discussion

4.1. As-built and annealed conditions

SEM observations of the as-built alloy revealed a hierarchical microstructure inside the melt pools (Fig. 1a), with coarse and elongated grains (Fig. 1c) composed of fine Al cells surrounded by a continuous Si network (Fig. 1b). XRD results (Fig. 5) show that the Si volumetric fraction was ~9.4%, which is much lower than the value predicted (11.7%) from the phase diagram. To clarify these results, EDX was conducted at a low accelerating voltage inside the Al cells of the as-built alloy, which indicated an average Si content of ~2.4 wt.% (the average was calculated from 10 readings). This value is much higher than the equilibrium value reported for AlSiMg alloys (<0.1%) and stems from the high solidification rate in the L-PBF process, estimated to be of the order of 10^3–10^6 °C/s [8]. Furthermore, the observed value is close to recently reported results [42]. Therefore, this value was set as the Si content (wt.%) in the Al solid solution and was used to generate the mass-balance equation. The densities of Si and Al phases and the corresponding binary alloy were set at 2.33, 2.7, and 2.68 g/cm^3, respectively, together with a total content of 10.24 wt.% for Si (Table 1). From the mass balance, a volumetric fraction of 9.3% was calculated for Si,

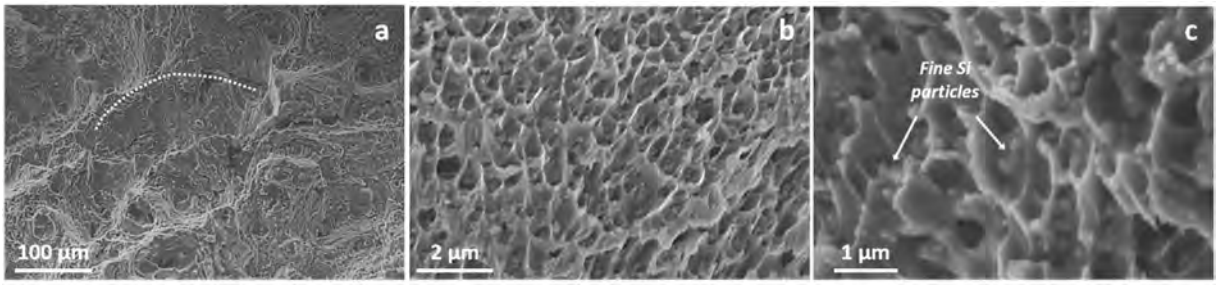

Fig. 8. Fracture surface of the AlSi10Mg alloy in the annealed condition (SE images): (a) panoramic view of the surface, the dotted line shows traces of the melt pool boundaries. (b) Fine equiaxed dimples. (c) Si particles emerging inside the dimples.

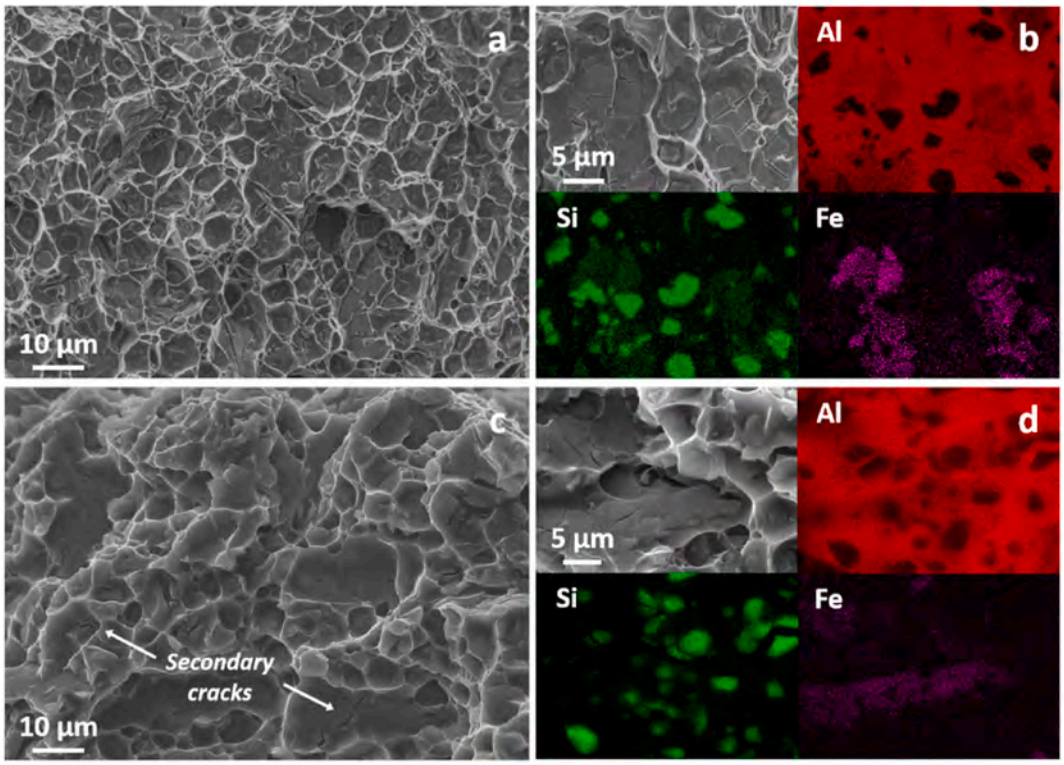

Fig. 9. Fracture surfaces of the AlSi10Mg alloy after high-temperature heat-treatment. (a) Without and (c) with the final ageing treatment. (b) and (d) EDX elemental mapping of Al, Si, and Fe from dimples in (a) and (c), respectively.

which is similar to the value obtained by Rietveld refinement. The noteworthy mechanical resistance of the as-built alloy, both in terms of impact strength and hardness, is likely related to the fine microstructures of the alloy and Si solid solution, rather than to the grain structure. On the contrary, the overall impact toughness is relatively low. As density measurements reveal a highly dense material, potential porosity cannot be held to be responsible for the low absorbed energy. Hence, the low absorbed energy is more related to the limited deformability of the as-built alloy, as suggested by the flat fracture surface in Fig. 7, and to possible residual internal stresses [32], dislocation networks [6], and solid-solution strengthening [42].

Annealing leads to the rupture of the Si network (Fig. 2a and b) but does not significantly modify the coarse grains (Fig. 2c). XRD analysis revealed that both the Al lattice parameters and Si volume fraction are restored to equilibrium values (Fig. 5b). The hardness of the alloy decreased to 87 HBW compared to its initial value, but its ductility, as suggested by the absorbed impact energy, increased significantly. This outcome agrees with the ductile dimple-like fracture surface in Fig. 8 and with the tensile behavior reported earlier [8,9,29]. Unlike hardness, the impact strengths of the annealed and as-built alloys were similar.

The contribution of each microstructural strengthening mechanism to the yield strength of the as-built and annealed alloys was calculated to better elucidate these findings. Five mechanisms were considered, namely grain boundaries (Hall-Petch), precipitates (Orowan), dislocations (Taylor), and solid-solution and load-bearing phase strengthening mechanisms. Table 4 shows the corresponding constitutive equations and numerical values and Fig. 10 graphically depicts the contribution of each mechanism.

Constant internal friction stress was observed in both alloys. The Hall-Petch effect was considered to originate from both Al cells and grains in the as-built alloy, while only the grains contributed to this effect in the annealed alloy [29]. The mean widths of the cells and grains reported in Section 3.1 were used to analyze the observed Hall-Petch relationship. Meanwhile, the overall volume fraction of nanometric Si particles was considered to contribute to Orowan strengthening in the annealed alloy, when the calculated ED was used as the particle size. Some studies reported the presence of nanometric Si precipitates in Al cells in the as-built alloy [6,45], but they were not detected in the present work (Fig. 1), probably due to differences in the process parameters employed. Therefore, there was no Orowan strengthening in the as-built

Table 4
Constitutive equations and the corresponding parameters for the yield strength estimation.

	Relationship		as-built	Annealed
Strengthening Mechanism	Internal Friction	σ_0	$\sigma_0 = 72\ MPa$ [43]	$\sigma_0 = 72\ MPa$ [43]
	Taylor	$\beta MGb\sqrt{\rho_d}$	$\beta = 0.16$ [6] $M = 3.06$ [44] $G = 27000\ MPa$ $b = 0.286\ nm$ [44] $\rho_d = 1.14{\cdot}10^{14}\ m^{-2}$ [45]	–
	Hall-Petch	$\frac{k}{\sqrt{d_{cell}}} + \frac{k}{\sqrt{d_{grain}}}$	$k = 40\ MPa{\cdot}\mu m^{0.5}$ [46] $d_{cell} = 0.4 \pm 0.05\ \mu m$ $d_{grain} = 7.5 \pm 1\ \mu m$	$k = 40\ MPa{\cdot}\mu m^{0.5}$ [46] $d_{grain} = 7.5 \pm 1\ \mu m$
	Solid Solution	KC^N	$K = 13\ MPa{\cdot}at\%^{-1}$ [47] $C = 2.4 \pm 0.5\ a.t.\%$ $N = 1$ [47]	$K = 13\ MPa{\cdot}at\%^{-1}$ [47] $C = 0.5\ a.t.\%$ [48] $N = 1$ [47]
	Orowan	$\frac{\phi Gb}{d_{Si}}{\cdot}\left(\frac{6V_{Si}}{\pi}\right)^{1/3}$	–	$\phi = 0.4$ [49] $d_{Si} = 92 \pm 7\ nm$ $V_{Si} = 0.117 \pm 0.003$
	Load-bearing phase	$1.5{\cdot}\sigma_i{\cdot}V_{Si}$	$\sigma_i = 240\ MPa$ [50] $V_{Si} = 0.094 \pm 0.004$	$\sigma_i = 240\ MPa$ [50] $V_{Si} = 0.117 \pm 0.003$
Estimation of Yield Strength	Cahoon [t]	$\left(\frac{HBW}{3}\right)(0.1)^n{\cdot}9.81$	$HBW = 125 \pm 1$ $n = 0.2$ [7]	$HBW = 87 \pm 1$ $n = 0.2$ [7]

alloy, as the Si phase was involved either in the eutectic network or in solid-solution strengthening. To analyze the latter, the amount of Si measured by EDX was used. The Taylor strengthening mechanism was supposed to be active only in the as-built alloy, assuming that this dislocation network can be recovered by annealing. In the load-bearing phase mechanism, a constant Si/Al interface strength was used.

As shown in Fig. 10, the calculated yield strength of the annealed alloy (155 ± 2 MPa) was 35% lower than that of the as-built alloy (255 ± 8 MPa). For comparison, experimental values of YS from tensile tests of the as-built (251 ± 6 MPa) and annealed (151 ± 6 MPa) samples were taken from a previous work by the authors [22]. Additionally, YS was also estimated from hardness measurements according to the relationship proposed by Cahoon et al. [51] (Table 4). A constant value of 0.2 was used for the strain-hardening coefficient *n*. The estimated values are 258 ± 2 MPa and 180 ± 2 MPa for the as-built and annealed alloys, respectively.

Fig. 10 shows that there is an excellent agreement between all values related to the as-built alloy. Calculated and experimental tensile values also match for the annealed alloy, whereas the value estimated from hardness is ~25–30 MPa higher. Despite such difference, the strength of the annealed alloy (either experimental, calculated or estimated) was significantly different from that of the as-built alloy. Hence, the numerical results obtained from microstructural observations better agree with hardness and tensile measurements rather than impact tests.

Such a discrepancy might be attributed to the lack of strain-rate dependency in the constitutive equations. Even though there is not much information available, some authors report a relationship between the microstructure and the corresponding strain-rate sensitivity of the alloy. Das et al. [52] showed that steel of different grades displays different responses with respect to strain rate. Similarly, Alturk et al. [53] verified that strain-rate sensitivity is remarkably high in ferritic and austenitic steels, while only a limited difference between quasi-static and high strain-rate tests characterizes dual-phase steels. Millet [54] studied the shock-loading response of a 6061 Al alloy in solution-treated and T6 conditions. As expected, the T6 alloy displayed an increase in strength during quasi-static testing as compared to solution-treated alloys due to ageing. Conversely, these alloys exhibited a similar response in shock-loading tests, with the material in the T6 state not showing any strain-rate sensitivity. Millet attributed such behavior to differences in the initial microstructure of the alloys. It is likely that the discrepancy between the as-built and annealed alloys in terms of impact and hardness can be explained similarly. Dislocation movement in the as-built alloy is strongly hindered by the increased solid-solution content and the high number of pre-existing defects, such as grain boundaries and dislocation tangles [45]. Hence, relatively few new dislocations are generated during the deformation process, and consequently, the

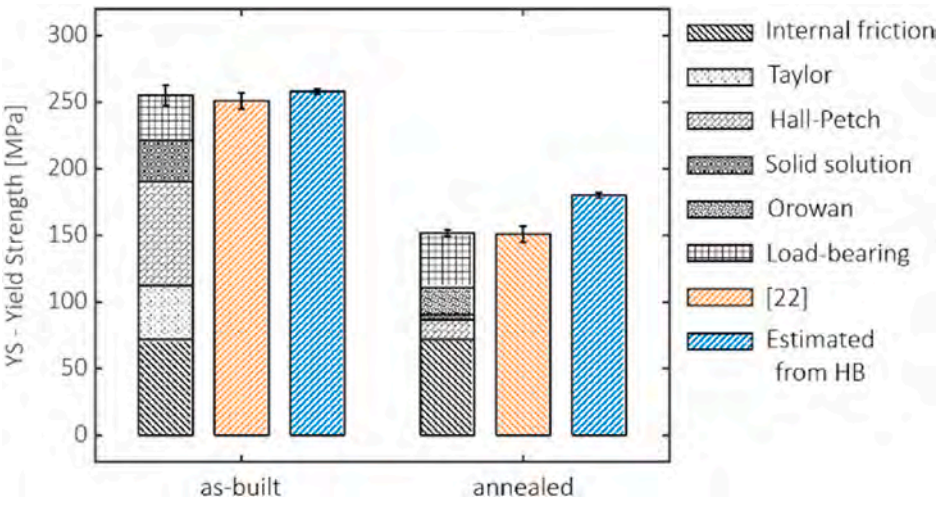

Fig. 10. Microstructural contributions to yield strength of the as-built and annealed alloys.

strain-rate sensitivity is rather low. Conversely, the relatively weak microstructure of the annealed alloy could be easily deformed, with a significant formation and movement of new dislocations. In impact tests, owing to the different strain rate sensitivities, similar impact strengths are observed for the annealed and as-built alloys; however, significant differences in strength are observed from quasi-static hardness tests. Further TEM investigations regarding microstructural evolution after impact tests are required for a deeper understanding of this phenomenon.

4.2. HIP- and heat-treated alloys

The T6 heat treatment reduced the relative density of the as-built alloy from 99.8% to 97.8%, due to growth of the pre-existing pores at high temperatures (Fig. 3d). In the present study, the presence of keyhole and lack-of fusion pores can be considered to be negligible as the process parameters were optimized. However, some small pores (few microns in size) might form during the AM process due to the entrapment of the inert shielding gas or by moisture absorption. At the high temperatures of the T6 heat treatment, the reduced material strength and increased gas pressure allowed the pores to grow significantly, as depicted in Fig. 3d, which consequently reduced material density and affected mechanical properties.

HIP treatment results in effective densification, regardless of the applied pressure, with the relative density of HIP, HPT6, and HIP + T6 alloys always being higher than 99%. Nonetheless, the exposure to high temperatures coarsened the Si particles and promoted needle-like Fe-rich compounds. Additionally, the absence of a subsequent ageing treatment indicates that strengthening compounds are not formed. These observations align with the limited impact strength (~5.5 kN), and hardness (~80 HBW) of the HIP treated samples and explains their high total absorbed energy (~10 J) and ductile behavior (Fig. 9a).

After HIP, HPT6 samples were furtherly subjected to ageing under high pressure, which is expected to affect the precipitation behavior, owing to the low employed temperature. The diffusion coefficient D depends on temperature and pressure, according to Ref. [55]:

$$D = D_0 e^{-\left(\frac{\Delta H}{RT}\right)} = D_0 e^{-\left(\frac{\Delta U + P\Delta V}{RT}\right)} \quad (1)$$

where D_0 is a pre-exponential factor, ΔH is the enthalpy change, ΔU is the activation energy of the diffusion process at atmospheric pressure, P is the relative pressure, ΔV is the activation volume. If both D_0 and ΔU are independent of pressure, and assuming a reasonable value of ΔV for strengthening compounds in Al alloys (~10^4 mm^3/mol [55]), the diffusion coefficient during ageing performed at $T = 453$ K (180 °C) and $P = 150$ MPa is ~2/3 of the diffusion coefficient at atmospheric pressure. Additionally, the high pressure raises the transformation temperatures of Al alloys with a baric coefficient of ~6–11 °C/100 MPa [56], which should reduce the driving force for precipitation.

The strength contributions of microstructural features of the HPT6 samples were calculated to deepen the microstructure-properties relationship. While SEM images showed similar grains to that of as-built and annealed samples, TEM investigations revealed a complex sub-grain structure. The contrast modulation in BF TEM images (Fig. 4b–c) and stretched spots in the DP pattern (Fig. 4d) suggest that the sub-grain structure is composed of dislocation boundaries, which reinforce the alloy by the Taylor mechanism. The area of the dislocation boundaries per unit volume ρ_d [m^{-1}] can be estimated as $2/L$ [29], where L is the mean length of sub-grains, assumed as ~200 nm from TEM investigations (Fig. 4). Using constants listed in Table 4, the strengthening contribution from dislocation boundaries is ~38 MPa, the Hall-Petch reinforcement from elongated grains ($d_{grain} = 7.5 \pm 1$ μm - Table 4) is ~15 MPa, and the Orowan contribution from Si particles ($V_{Si} = 0.117 \pm 0.003$ - Fig. 5, $d_{Si} = 1.2 \pm 0.9$ μm - § 3.1) is negligible (~2 MPa) due to their micrometric size.

TEM investigations also highlighted nanometric compounds (Fig. 4e–f), ranging between ~4 and 10 nm in size (§ 3.2). Using constants listed in Table 4, their strengthening contribution by the Orowan relationship, assuming a mean diameter of ~7 nm and a typical volumetric fraction of ~1% [39], is ~118 MPa. Additionally, owing to their coherency with the Al lattice (Fig. 4e), the interface strength should be in the order of ~700–1000 MPa [57], giving a load-bearing reinforcement of ~10–15 MPa. The addition of all contributes reported above to the internal friction (72 MPa - Table 4) yields a calculated strength of ~254 MPa. This value reasonably matches the tensile properties of both HPT6 and HIP + T6 samples (252 MPa and 261 MPa, respectively [22]). Furthermore, it agrees with their increased impact strength (~6.6–7.2 kN) and hardness (~100–110 HBW) as compared to the only HIP treated samples. This simplified analysis suggests that, regardless of the higher pressure of the HPT6 treatment, precipitation was prolific and microstructure was comparable in both HPT6 and HIP + T6 alloys, which agrees with their similar impact and hardness properties.

Beside impact strength, HPT6 and HIP + T6 samples also shared limited absorbed energy. Nanometric ageing-induced compounds are associated with a local strain field at the interface owing to lattice misfit with the parent Al matrix [39]. Consequently, resistance to further deformation and fracture propagation is severely affected, especially at high strain rates. Despite this, fracture surfaces still showed a dimples-like appearance (Fig. 9c), which indicates the primary role of Si in damage nucleation and fracture behavior. It is worth to note that the exposure to high temperatures also promoted plate-like Fe-based compounds, whose brittleness affects energy absorption and fracture behavior negatively. However, the reduced volumetric fraction (~0.66–0.83%) and micrometric size reasonably hide their effect as compared to Si particles and strengthening compounds in both HIP- and ageing-treated samples. In this light, they were not considered in the analyses reported above.

Despite the different processing route, HPT6 and HIP + T6 samples showed a similar microstructure. The analysis of strengthening contributions from microstructural features supported this observation in light of static and impact properties, which were comparable for both heat treatment conditions. Further studies considering different ageing temperatures and soaking times will be performed to verify the current results to be generally applicable. However, the present outcomes satisfactorily supported the assumption that the HPT6 treatment could be a suitable candidate for a possible replacement of the conventional HIP + T6 route, thus leading to significant technological advantages.

5. Concluding remarks

In this work, the impact and microstructural properties of L-PBF AlSi10Mg alloys subjected to different heat-treatment conditions were analyzed. A new route that combines HIP and ageing under pressure (HPT6) was applied and the resultant impact behavior of the alloy was investigated. The impact properties of the same alloy after low-temperature annealing and conventional T6 treatment were also studied for comparison. The following conclusions could be drawn from our observations.

- The as-built alloy is characterized by a hierarchical microstructure consisting of coarse columnar grains and smaller Al cells, which are surrounded by a Si network. XRD analysis indicated the existence of non-equilibrium conditions due to a large amount of Si retained in the solid solution. This microstructure accounts for the remarkable impact strength of the as-built alloy but together with process-related defects, it is also responsible for the low impact toughness of the material.
- Low-temperature annealing completely restored the equilibrium conditions of the alloy. The Si network dissolved and formed nanometric Si particles, while coarse grains were not significantly affected. Changes in the microstructure reduce the static strength of the alloy, as measured by hardness tests. Conversely, impact strength

and toughness of this alloy were the best among all the investigated conditions. This is likely due to a different material response in quasi-static or in rapid loading conditions. In this light, low-temperature annealing is a valuable alternative to achieve equilibrium conditions, reasonable static properties and excellent impact behavior. However, high-temperature treatment is required to match static and impact properties.

- HIP before heat treatment resulted in a significant densification in the alloy as compared to T6 heat treatment alone. It should be noted that high-density and defect-free products are recommended, especially when high impact and fatigue resistance are required. However, the high HIP temperature strongly affects the microstructure of the alloy owing to which its hardness and impact strength are reduced. These can be restored by ageing treatment at the expense of ductility and absorbed energy.
- TEM analysis of the HPT6 alloy revealed the inclusion of nanometric precipitates, thus demonstrating that the novel route is capable of inducing precipitation strengthening in the AlSi10Mg alloy. Additionally, it results in a mechanical performance very similar to that of the standard HIP + T6 route, supporting the fact that HPT6 can possibly replace HIP + T6. The elimination of solution heat treatment will simultaneously cut down the processing duration and cost of production of L-PBF AlSi10Mg alloys.

Author contributions

MG performed the SEM and XRD characterization and corresponding data analysis. MT performed the annealing and T6 heat treatments, density measurements and hardness tests. AF conducted the Charpy impact tests; MG analyzed the corresponding data. MF and AM performed the TEM characterization; MF and MG analyzed the corresponding data. MM acquired funding and supervised the work. AP acquired the additively manufactured specimens and HIP treatments, and supervised the work. MG and MT wrote the first draft of the manuscript. All authors contributed to reviewing and editing the manuscript and discussing and interpreting all the results.

Funding

This work was partially funded by the University Found for the Scientific Research (FAR) 2019 of the University of Ferrara (Italy).

Data availability

The data that support the findings of this study are available from the corresponding author on reasonable request.

Declaration of competing interest

The authors declare that they have no known competing financial interests or personal relationships that could have appeared to influence the work reported in this paper.

Acknowledgment

The authors gratefully acknowledge Mr J. Shipley and Mr J. Gårdstam (Quintus Technologies AB) for their help with HIP treatment, Dr. L. Girelli for the valuable technical support, and Mr. G. Bertocchi for help in XRD testing. The authors further thank Dr. A. Balbo and Dr. L. Lattanzi for their support and advice related to SEM analysis.

References

[1] J.R. Davis (Ed.), ASM Speciality Handbook: Aluminum and Aluminum Alloys, ASM International, 1993.
[2] T. DebRoy, H.L. Wei, J.S. Zuback, T. Mukherjee, J.W. Elmer, J.O. Milewski, A. M. Beese, A. Wilson-Heid, A. De, W. Zhang, Additive manufacturing of metallic components – process, structure and properties, Prog. Mater. Sci. 92 (2018) 112–224, https://doi.org/10.1016/j.pmatsci.2017.10.001.
[3] X. Niu, S. Singh, A. Garg, H. Singh, B. Panda, X. Peng, Q. Zhang, Review of materials used in laser-aided additive manufacturing processes to produce metallic products, Front. Mech. Eng. 14 (2019) 282–298.
[4] N.T. Aboulkhair, M. Simonelli, L. Parry, I. Ashcroft, C. Tuck, R. Hague, 3D printing of Aluminium alloys: additive Manufacturing of Aluminium alloys using selective laser melting, Prog. Mater. Sci. 106 (2019), 100578, https://doi.org/10.1016/j.pmatsci.2019.100578.
[5] D. Buchbinder, H. Schleifenbaum, S. Heidrich, W. Meiners, J. Bültmann, High power selective laser melting (HP SLM) of aluminum parts, Phys. Procedia. 12 (2011) 271–278, https://doi.org/10.1016/j.phpro.2011.03.035.
[6] A. Hadadzadeh, B.S. Amirkhiz, M. Mohammadi, Contribution of Mg2Si precipitates to the strength of direct metal laser sintered AlSi10Mg, Mater. Sci. Eng. 739 (2019) 295–300, https://doi.org/10.1016/j.msea.2018.10.055.
[7] L. Zhou, A. Mehta, E. Schulz, B. McWilliams, K. Cho, Y. Sohn, Microstructure, precipitates and hardness of selectively laser melted AlSi10Mg alloy before and after heat treatment, Mater. Char. 143 (2018) 5–17, https://doi.org/10.1016/j.matchar.2018.04.022.
[8] X.P. Li, X.J. Wang, M. Saunders, A. Suvorova, L.C. Zhang, Y.J. Liu, M.H. Fang, Z. H. Huang, T.B. Sercombe, A selective laser melting and solution heat treatment refined Al-12Si alloy with a controllable ultrafine eutectic microstructure and 25% tensile ductility, Acta Mater. 95 (2015) 74–82, https://doi.org/10.1016/j.actamat.2015.05.017.
[9] L. Zhuo, Z. Wang, H. Zhang, E. Yin, Y. Wang, T. Xu, C. Li, Effect of post-process heat treatment on microstructure and properties of selective laser melted AlSi10Mg alloy, Mater. Lett. 234 (2019) 196–200, https://doi.org/10.1016/j.matlet.2018.09.109.
[10] J. Fiocchi, A. Tuissi, P. Bassani, C.A. Biffi, Low temperature annealing dedicated to AlSi10Mg selective laser melting products, J. Alloys Compd. 695 (2017) 3402–3409, https://doi.org/10.1016/j.jallcom.2016.12.019.
[11] I. Rosenthal, R. Shneck, A. Stern, Heat treatment effect on the mechanical properties and fracture mechanism in AlSi10Mg fabricated by additive manufacturing selective laser melting process, Mater. Sci. Eng. 729 (2018) 310–322, https://doi.org/10.1016/j.msea.2018.05.074.
[12] N.T. Aboulkhair, I. Maskery, C. Tuck, I. Ashcroft, N.M. Everitt, The microstructure and mechanical properties of selectively laser melted AlSi10Mg: the effect of a conventional T6-like heat treatment, Mater. Sci. Eng. 667 (2016) 139–146, https://doi.org/10.1016/j.msea.2016.04.092.
[13] L.F. Wang, J. Sun, X.L. Yu, Y. Shi, X.G. Zhu, L.Y. Cheng, H.H. Liang, B. Yan, L. J. Guo, Enhancement in mechanical properties of selectively laser-melted AlSi10Mg aluminum alloys by T6-like heat treatment, Mater. Sci. Eng. 734 (2018) 299–310, https://doi.org/10.1016/j.msea.2018.07.103.
[14] C. Weingarten, D. Buchbinder, N. Pirch, W. Meiners, K. Wissenbach, R. Poprawe, Formation and reduction of hydrogen porosity during selective laser melting of AlSi10Mg, J. Mater. Process. Technol. 221 (2015) 112–120, https://doi.org/10.1016/j.jmatprotec.2015.02.013.
[15] L. Girelli, M. Tocci, M. Gelfi, A. Pola, Study of heat treatment parameters for additively manufactured AlSi10Mg in comparison with corresponding cast alloy, Mater. Sci. Eng. 739 (2019) 317–328, https://doi.org/10.1016/j.msea.2018.10.026.
[16] C.B. Finfrock, A. Exil, J.D. Carroll, L. Deibler, Effect of hot isostatic pressing and powder feedstock on porosity, microstructure, and mechanical properties of selective laser melted AlSi10Mg, Metallogr. Microstruct. Anal. 7 (2018) 443–456, https://doi.org/10.1007/s13632-018-0456-z.
[17] N.E. Uzan, R. Shneck, O. Yeheskel, N. Frage, Fatigue of AlSi10Mg specimens fabricated by additive manufacturing selective laser melting (AM-SLM), Mater. Sci. Eng. 704 (2017) 229–237, https://doi.org/10.1016/j.msea.2017.08.027.
[18] U. Tradowsky, J. White, R.M. Ward, N. Read, W. Reimers, M.M. Attallah, Selective laser melting of AlSi10Mg: influence of post-processing on the microstructural and tensile properties development, Mater. Des. 105 (2016) 212–222, https://doi.org/10.1016/j.matdes.2016.05.066.
[19] T. Hirata, T. Kimura, T. Nakamoto, Effects of hot isostatic pressing and internal porosity on the performance of selective laser melted AlSi10Mg alloys, Mater. Sci. Eng. 772 (2020) 138713, https://doi.org/10.1016/j.msea.2019.138713.
[20] W.H. Kan, Y. Nadot, M. Foley, L. Ridosz, G. Proust, J.M. Cairney, Factors that affect the properties of additively-manufactured AlSi10Mg: porosity versus microstructure, Addit. Manuf. 29 (2019), 100805, https://doi.org/10.1016/j.addma.2019.100805.
[21] S. Hafenstein, E. Werner, Pressure dependence of age-hardenability of aluminum cast alloys and coarsening of precipitates during hot isostatic pressing, Mater. Sci. Eng. 757 (2019) 62–69, https://doi.org/10.1016/j.msea.2019.04.077.
[22] M. Tocci, A. Pola, M. Gelfi, G.M. La Vecchia, Effect of a new high-pressure heat treatment on additively manufactured AlSi10Mg alloy, Metall. Mater. Trans. A Phys. Metall. Mater. Sci. (2020), https://doi.org/10.1007/s11661-020-05905-y.
[23] S. Tammas-Williams, P.J. Withers, I. Todd, P.B. Prangnell, Porosity regrowth during heat treatment of hot isostatically pressed additively manufactured titanium components, Scripta Mater. 122 (2016) 72–76, https://doi.org/10.1016/j.scriptamat.2016.05.002.
[24] E. Padovano, C. Badini, A. Pantarelli, F. Gili, F. D'Aiuto, A comparative study of the effects of thermal treatments on AlSi10Mg produced by laser powder bed fusion, J. Alloys Compd. 831 (2020), 154822, https://doi.org/10.1016/j.jallcom.2020.154822.
[25] K. Kempen, L. Thijs, J. Van Humbeeck, J.P. Kruth, Mechanical properties of AlSi10Mg produced by selective laser melting, Phys. Procedia. 39 (2012) 439–446, https://doi.org/10.1016/j.phpro.2012.10.059.

[26] L. Girelli, M. Giovagnoli, M. Tocci, A. Pola, A. Fortini, M. Merlin, G.M. La Vecchia, Evaluation of the impact behaviour of AlSi10Mg alloy produced using laser additive manufacturing, Mater. Sci. Eng. 748 (2019) 38–51, https://doi.org/10.1016/j.msea.2019.01.078.
[27] L. Lattanzi, A. Fortini, M. Giovagnoli, M. Merlin, Influence of Mg and Ti on both eutectic solidification and modifying efficiency in Sr-modified Al-7Si cast alloys, Metall. Ital. 110 (2018) 5–15.
[28] L. Lutterotti, H.R. Wenk, S. Matthies, MAUD (material analysis using diffraction): a user friendly Java program for Rietveld texture analysis and more, in: ICOTOM-12, 1999, pp. 1599–1604.
[29] N. Takata, H. Kodaira, K. Sekizawa, A. Suzuki, M. Kobashi, Change in microstructure of selectively laser melted AlSi10Mg alloy with heat treatments, Mater. Sci. Eng. 704 (2017) 218–228, https://doi.org/10.1016/j.msea.2017.08.029.
[30] M. Fousová, D. Dvorský, A. Michalcová, D. Vojtěch, Changes in the microstructure and mechanical properties of additively manufactured AlSi10Mg alloy after exposure to elevated temperatures, Mater. Char. 137 (2018) 119–126, https://doi.org/10.1016/j.matchar.2018.01.028.
[31] Y.H. Cho, H.C. Lee, K.H. Oh, A.K. Dahle, Effect of strontium and phosphorus on eutectic Al-Si nucleation and formation of β-Al5FeSi in hypoeutectic Al-Si foundry alloys, Metall. Mater. Trans. A Phys. Metall. Mater. Sci. 39 (2008) 2435–2448, https://doi.org/10.1007/s11661-008-9580-8.
[32] A.H. Maamoun, M. Elbestawi, G.K. Dosbaeva, S.C. Veldhuis, Thermal post-processing of AlSi10Mg parts produced by Selective Laser Melting using recycled powder, Addit. Manuf. 21 (2018) 234–247, https://doi.org/10.1016/j.addma.2018.03.014.
[33] T. Tański, P. Snopiński, Effect of the processing conditions on the microstructural features and mechanical behavior of aluminum alloys, in: Alum. Alloy. Recent Trends Process. Charact. Mech. Behav. Appl, 2017, pp. 137–156.
[34] Y. Chen, Y. Tang, H. Zhang, N. Hu, N. Gao, M.J. Starink, Microstructures and hardness prediction of an ultrafine-grained al-2024 alloy, Metals 9 (2019) 1–10, https://doi.org/10.3390/met9111182.
[35] J. Lu, Y. Zhao, Y. Du, W. Zhang, Y. Zhang, Microstructure and mechanical properties of a novel titanium alloy with homogeneous (TiHf)5Si3 article-reinforcements, J. Alloys Compd. 778 (2019) 115–123, https://doi.org/10.1016/j.jallcom.2018.11.117.
[36] S.J. Andersen, C.D. Marioara, R. Vissers, A. Frøseth, H.W. Zandbergen, The structural relation between precipitates in Al-Mg-Si alloys, the Al-matrix and diamond silicon, with emphasis on the trigonal phase U1-MgAl2Si2, Mater. Sci. Eng. 444 (2007) 157–169, https://doi.org/10.1016/j.msea.2006.08.084.
[37] S.J. Andersen, H.W. Zandbergen, J. Jansen, C. Træholt, U. Tundal, O. Reiso, The crystal structure of the β″ phase in Al-Mg-Si Alloys, Acta Mater. 46 (1998) 3283–3298, https://doi.org/10.1016/S1359-6454(97)00493-X.
[38] H. Chen, J. Lu, Y. Kong, K. Li, T. Yang, A. Meingast, M. Yang, Q. Lu, Y. Du, Atomic scale investigation of the crystal structure and interfaces of the B′ precipitate in Al-Mg-Si alloys, Acta Mater. 185 (2020) 193–203, https://doi.org/10.1016/j.actamat.2019.11.059.
[39] H.W. Zandbergen, S.J. Andersen, J. Jansen, Structure determination of Mg5Si6: particles in Al by dynamic electron diffraction studies, Science 277 (1997) 1221–1225, https://doi.org/10.1126/science.277.5330.1221, 80.
[40] J.H. Rao, Y. Zhang, K. Zhang, A. Huang, C.H.J. Davies, X. Wu, Multiple precipitation pathways in an Al-7Si-0.6Mg alloy fabricated by selective laser melting, Scripta Mater. 160 (2019) 66–69, https://doi.org/10.1016/j.scriptamat.2018.09.045.
[41] S. Marola, D. Manfredi, G. Fiore, M.G. Poletti, M. Lombardi, P. Fino, L. Battezzati, A comparison of Selective Laser Melting with bulk rapid solidification of AlSi10Mg alloy, J. Alloys Compd. 742 (2018) 271–279, https://doi.org/10.1016/j.jallcom.2018.01.309.
[42] T. Maeshima, K. Oh-ishi, Solute clustering and supersaturated solid solution of AlSi10Mg alloy fabricated by selective laser melting, Heliyon 5 (2019), e01186, https://doi.org/10.1016/j.heliyon.2019.e01186.
[43] E. Ghassemali, M. Riestra, T. Bogdanoff, B.S. Kumar, S. Seifeddine, Hall-Petch equation in a hypoeutectic Al-Si cast alloy: grain size vs. secondary dendrite arm spacing, Procedia Eng 207 (2017) 19–24, https://doi.org/10.1016/j.proeng.2017.10.731.
[44] B. Chen, S.K. Moon, X. Yao, G. Bi, J. Shen, J. Umeda, K. Kondoh, Strength and strain hardening of a selective laser melted AlSi10Mg alloy, Scripta Mater. 141 (2017) 45–49, https://doi.org/10.1016/j.scriptamat.2017.07.025.
[45] A. Hadadzadeh, B. Shalchi Amirkhiz, A. Odeshi, J. Li, M. Mohammadi, Role of hierarchical microstructure of additively manufactured AlSi10Mg on dynamic loading behavior, Addit. Manuf. 28 (2019) 1–13, https://doi.org/10.1016/j.addma.2019.04.012.
[46] N. Hansen, Hall–Petch relation and boundary strengthening, Scripta Metall. 51 (2005) 801–806.
[47] Q. Zhao, B. Holmedal, The effect of silicon on the strengthening and work hardening of aluminum at room temperature, Mater. Sci. Eng. 563 (2013) 147–151, https://doi.org/10.1016/j.msea.2012.11.062.
[48] V.C. Pierre, B. Anthony, T. Lore, V.H. Brecht, V. Kim, Heat treatment optimization via thermo-physical characterization of AlSi7Mg and AlSi10Mg manufactured by laser powder bed fusion (LPBF), Euro PM 2018 Congr, Exhib (2020) 1–7.
[49] E.D. Cyr, A. Brahme, M. Mohammadi, R.K. Mishra, K. Inal, A new crystal plasticity framework to simulate the large strain behaviour of aluminum alloys at warm temperatures, Mater. Sci. Eng. 727 (2018) 11–28.
[50] S. Xia, Y. Qi, T. Perry, K.S. Kim, Strength characterization of Al/Si interfaces: a hybrid method of nanoindentation and finite element analysis, Acta Mater. 57 (2009) 695–707, https://doi.org/10.1016/j.actamat.2008.10.011.
[51] J.R. Cahoon, W.H. Broughton, A.R. Kutzak, The determination of yield strength from hardness measurements, Metall. Trans. 2 (1971) 1979–1983, https://doi.org/10.1177/0963947016674142.
[52] A. Das, P. Biswas, S. Tarafder, D. Chakrabarti, S. Sivaprasad, Effect of strengthening mechanism on strain-rate related tensile properties of low-carbon sheet steels for automotive application, J. Mater. Eng. Perform. 27 (2018) 3709–3722, https://doi.org/10.1007/s11665-018-3405-8.
[53] R. Alturk, S. Mates, Z. Xu, F. Abu-Farha, Effects of microstructure on the strain rate sensitivity of advanced steels, in: Miner. Met. Mater. Ser., 2017, pp. 243–254, https://doi.org/10.1007/978-3-319-51493-2_24.
[54] J.C.F. Millett, Modifications of the response of materials to shock loading by age hardening, Metall. Mater. Trans. A Phys. Metall. Mater. Sci. 46 (2015) 4506–4517, https://doi.org/10.1007/s11661-014-2571-z.
[55] T. Evans, E. Williams, Effect of pressure on precipitation in an Al-4·3% Cu alloy, Philos. Mag. A 20 (1969) 181–194, https://doi.org/10.1080/14786436908228545.
[56] T.K. Akopyan, N.A. Belov, A.G. Padalko, N.V. Letyagin, N.N. Avksent'yeva, Analysis of the effect of hydrostatic pressure on the nonvariant eutectic transformation in Al–Si, Al–Cu, and Al–Cu–Si systems, Phys. Met. Metallogr. 120 (2019) 593–599, https://doi.org/10.1134/S0031918X19060024.
[57] X.P. Li, G. Ji, Z. Chen, A. Addad, Y. Wu, H.W. Wang, J. Vleugels, J. Van Humbeeck, J.P. Kruth, Selective laser melting of nano-TiB2decorated AlSi10Mg alloy with high fracture strength and ductility, Acta Mater. 129 (2017) 183–193, https://doi.org/10.1016/j.actamat.2017.02.062.